Journal of Power Sources 207 (2012) 205–211

Contents lists available at SciVerse ScienceDirect

Journal of Power Sources

journal homepage: www.elsevier.com/locate/jpowsour

Monitoring electroactive ions at manganese dioxide pseudocapacitive electrodes with scanning electrochemical microscope for supercapacitor electrodes

Afriyanti Sumboja [a], Ushula Mengesha Tefashe [b], Gunther Wittstock [b], Pooi See Lee [a,*]

[a] School of Materials Science and Engineering, Nanyang Technological University, 50 Nanyang Avenue, Singapore 639798, Singapore
[b] Carl von Ossietzky University of Oldenburg, Center of Interface Science, Department of Pure and Applied Chemistry, D-26111 Oldenburg, Germany

ARTICLE INFO

Article history:
Received 29 November 2011
Received in revised form 29 January 2012
Accepted 30 January 2012
Available online 7 February 2012

Keywords:
Manganese dioxide
Kinetics process
Scanning electrochemical microscopy
Charge transfer
Supercapacitor

ABSTRACT

Hierarchical nanostructures of hydrated α-manganese dioxide (MnO_2) are prepared and their kinetics properties are characterized using scanning electrochemical microscopy (SECM). The SECM measurements are focused on the feedback mode approach curve to extract the effective heterogeneous charge transfer rate constant and illustration of the ultramicroelectrode (UME) tip-substrate cyclic voltammetry. Positive feedback current is observed during the SECM approach curve, indicating the efficient charge transfer process into the MnO_2 electrode. These studies complement electrochemical impedance spectroscopy and charge discharge measurements that are carried out to determine the effectiveness of the resultant MnO_2 for supercapacitor application. Specific capacitance as high as 356 $F g^{-1}$ at 2 $A g^{-1}$ is achieved and there is no degradation of the capacitance after 2000 cycles of cycling test, indicating its good capacitive properties for supercapacitor application.

1. Introduction

Electrochemical characterizations for energy storage materials are mostly done on macroscopic or device level, which provide the average measurement across the area of the electrode. However, in many cases, thickness and chemical composition of the electrodes may not be uniform throughout the electrode surface; or it may contain microscopic features of interest, in particular, for nanostructured electrodes. In addition, some localized surface modifications affect the overall charge transfer process. In order to address the heterogeneity of the electrode materials, in depth examination on the microscopic or nanoscopic level is required, such as the detail of the charge transport processes and interfacial reactions [1,2]. This would allow correlating the structural and electrochemical properties, providing the clue in optimizing the morphology and understanding the possible failure mechanism of the electrodes materials.

Scanning electrochemical microscopy (SECM) provides insightful electrochemical characterization on localized and spatially resolved sub-micrometer scale investigation of a wide range of materials and interfaces [3–6]. The micrometer to nanometer size of a disk shaped ultramicroelectrode (UME), often called "tip", enables the measurement of fast interfacial processes within the small UME/sample gap with precise measurement and high spatial resolution. The measured faradaic current that flows through the UME in liquid medium is used to characterize the kinetics of the electrochemical process of the sample. In the feedback mode, one form of a quasi-reversible redox couple is added as mediator to the working solution. This compound is electrolyzed at the UME. The magnitude of the UME current depends on the electron transfer kinetics for the mediator regeneration at the sample surface, which is related to the conductivity and electron transfer kinetics of the sample, as well as to the mass transfer processes in the solution [7,8]. Feedback mode measurements are useful to investigate the heterogeneous electron transfer kinetics process, including the quantification of the effective charge transfer rate constant and redox behavior of the sample [9]. These have been used earlier to characterize electron transfer processes at laterally structured samples ITO [4] and to study insertion and ejection processes of cations or anions into films of WO_3 [10], networks of carbon nanotubes [11], and polypyrrole layers [3]. The UME cyclic voltammetry is also useful for investigating the localized steady state voltammetric response of the sample, providing insights on the microscopic ion transport process as well as surface reactivity of the sample [12–14].

Charge transfer kinetics process is particularly important for electrochemical systems such as fuel cell, batteries, solar cell, chemical sensor, supercapacitor, etc. Investigation of the charge transfer across the interfaces by using SECM technique has been introduced into various applications. SECM has been used to study the charge transfer kinetics between the photo-oxidized dye molecules and iodide ion in dye-sentitized solar cell (DSSC) [15,16]. It is also

* Corresponding author. Tel.: +65 6790 6661; fax: +65 6790 9081.
E-mail address: PSLee@ntu.edu.sg (P.S. Lee).

0378-7753/$ – see front matter © 2012 Elsevier B.V. All rights reserved.
doi:10.1016/j.jpowsour.2012.01.153

applicable to investigate the kinetics process during the hydrogen evolution reaction which is the basic process for hydrogen generation on the electrocatalytic electrodes in fuel cell [6,17]. Furthermore, SECM has been utilized to characterize the charge transfer properties at the interface of electrode and new type of electrolyte such as room temperature ionic liquid (RTIL) [5,18].

Manganese dioxide (MnO_2) is one of the pseudocapacitive electrode materials that has a wide range of crystallographic structures and several oxidation states. Electrochemical properties of MnO_2 have been subjected to extensive studies due to its potential application for electrochemical energy storage devices, such as batteries and supercapacitors [19–21]. The pioneering work of MnO_2 as supercapacitor electrode was introduced by Lee and Goodenough [22,23]. Despite substantial studies on the effect of the morphology, crystallography, surface area and pore structure on the capacitive properties of MnO_2, less attention has been paid to the kinetics and charge transfer capabilities of the MnO_2 nanostructures. The kinetics of this material is clearly important for its role in energy storage and conversion. For example, electrolyte cations diffusion in the MnO_2 bulk structures has been shown to affect the optimum thickness of the electrode as well as specific capacitance of the MnO_2 [24]. Besides cations diffusion, electron conductivity plays an important role in optimizing the electrochemical reactivity and specific capacitance of MnO_2. Variation in the microstructures of MnO_2 has been reported to affect its electron conductivity and cations mobility [25].

In our previous work, we have synthesized hydrated α ultrathin MnO_2 nanostructures at room temperature and the morphological transformation into well-dispersed nanorods upon hydrothermal treatment [26]. In this work, we modify the synthesis method of ultrathin nanostructure using block copolymer template to increase the accessible surface area of the MnO_2 and measure the charge transfer kinetics using SECM. To the best of our knowledge, this is a first attempt in employing SECM to monitor redox probes on the high surface area nanostructured supercapacitor electrode. This provides insights on the facile charge transfer between the solution redox couples and the pseudocapacitive MnO_2 ultrathin nanostructures.

2. Experimental

2.1. Chemicals

P123 ($HO(CH_2CH_2O)_{20}(CH_2CH(CH_3)O)_{70}(CH_2CH_2O)_{20}H$), $KMnO_4$, poly(vinylidene fluoride) (PVDF), N-methylpyrrolidinone (NMP), carbon black, Na_2SO_4, $K_3[Fe(CN)_6]$, KNO_3 were purchased from Sigma–Aldrich. $Mn(NO_3)_2$ was purchased from Alfa Aesar. All of them were used as received. All aqueous solutions were prepared from deionized water (Milli-Q, Millipore Corp).

2.2. MnO_2 synthesis and electrode preparation

P123 (13.8 mmol) was dissolved in ethanol (10 mL). $Mn(NO_3)_2$ (13.8 mL, 0.1 M) and $KMnO_4$ (20 mL, 0.1 M) were added into the solution and stirred for 6 h at room temperature. The precipitates were centrifuged and washed with deionized water for several times and dried at 65 °C. Working electrodes were prepared by mixing the as-synthesized powder (85 wt%), carbon black (10 wt%), and PVDF (5 wt%). A few drops of NMP were added to form slurry. It was then coated on the carbon paper as current collector and dried under vacuum at 65 °C for 4 h. Typical thickness of the active materials of each sample was controlled within 18 ± 2 μm. The typical mass of each MnO_2 sample is about 0.3 ± 0.02 mg cm^{-2}.

2.3. Materials characterization and electrochemical testing

Morphologies of MnO_2 powders were investigated using scanning electron microscopy (SEM, JEOL-7600F) and transmission electron microscopy (TEM, JEOL 2010). Crystal structures of the MnO_2 powders were studied by X-ray diffractometer (Bruker D8 Advance). The specific surface area was measured using BET method based on physical absorption of nitrogen on automatic volumetric physisorption analyzer (ASAP 2020 Micrometrics). SECM measurements were performed on a home-built instrument [16]. The Teflon cell was equipped with a Pt (Goodfellow, Bad Nauheim, Germany) as counter electrode and an Ag (Goodfellow) as quasi-reference electrode (Ag QRE), MnO_2 substrate and UME were connected as working electrodes. The UME was fabricated by sealing Pt wires (25 μm diameter, Goodfellow, Bad Nauheim, Germany) into borosilicate glass capillaries (Hilgenberg GmbH, Malsfeld, Germany), followed by grinding the probe end. The UME tip has radius of 6.28 μm with *RG* of 14.95 (*RG* is the ratio of the glass sheath and the radius of the active UME tip). The mediator selected for this measurement was 1 mM $K_3[Fe(CN)_6]$ in 0.1 M KNO_3 supporting electrolyte. All the approach curves were performed at approach rate of 2 μm s^{-1}. The UME tip-substrate voltammetry was recorded with a CHI 7001B (CH Instruments, Austin, TX, USA) in a four electrode setup utilizing the aforementioned electrochemical setup. SECM feedback mode approach curves were acquired through SECMx software and the normalized approach curves were fitted to digital simulation of finite kinetics developed by Cornut and Lefrou [27] to extract the normalized heterogeneous first order rate constant κ ($\kappa = k_{eff} r_T/D$), where k_{eff} is the effective heterogeneous first order rate constant, D is the diffusion coefficient of the redox active mediator (i.e. $[Fe(CN)_6]^{3-}$). Electrochemical studies were also carried out by using Solartron, S1470E electrochemical interface. Three electrodes set up in 1 M Na_2SO_4 electrolyte were used, with platinum sheet and saturated Ag/AgCl as counter and reference electrode, respectively. Electrochemical impedance spectroscopy measurements were conducted at constant voltage mode (0.2 V vs. Ag/AgCl) by sweeping the frequency from 55 kHz to 10 mHz at an amplitude of 5 mV.

3. Results and discussion

3.1. Characterization of MnO_2

The synthesized MnO_2 powders have nanosphere-like morphology such as shown in Fig. 1a–c. At higher magnification, obvious asperities are visible on the surface of the spheres which consist of hierarchically assembled small ultrathin nanostructures. TEM observation confirms the presence of these ultrathin nanostructures with fine nanorod-like structures in diameter of 2–4 nm. The ultrathin nanostructures formation can be understood from the following growth mechanism. Micelles of P123 are formed when dissolved in ethanol. In the presence of $Mn(NO_3)_2$ precursor, Mn^{2+}–P123 complex will be formed [28]. Mn^{2+} would cover the micelle surface and penetrate into the PEO tails such as shown in Fig. 1d. Addition of $KMnO_4$ and assistance of NO_3^- as oxidizing agent oxidized the Mn^{2+} which subsequently promoted the nucleation of ultrathin nanostructure [26]. Highly porous structures were produced upon removal of P123. Due to the interaction of Mn^{2+}–P123 in the micelle form, the nucleation and growth of ultrathin nanostructures would occur only on the micelles. The small micelles lead to the formation of nanospheres within 100 nm in diameter. Nucleation of Mn^{2+} ions on the micelles occurred instantaneously, enabling the isolated growth of nanospheres consisting of 2–4 nm fine nanorods. In the absence of P123 micelle, Mn^{2+} ions

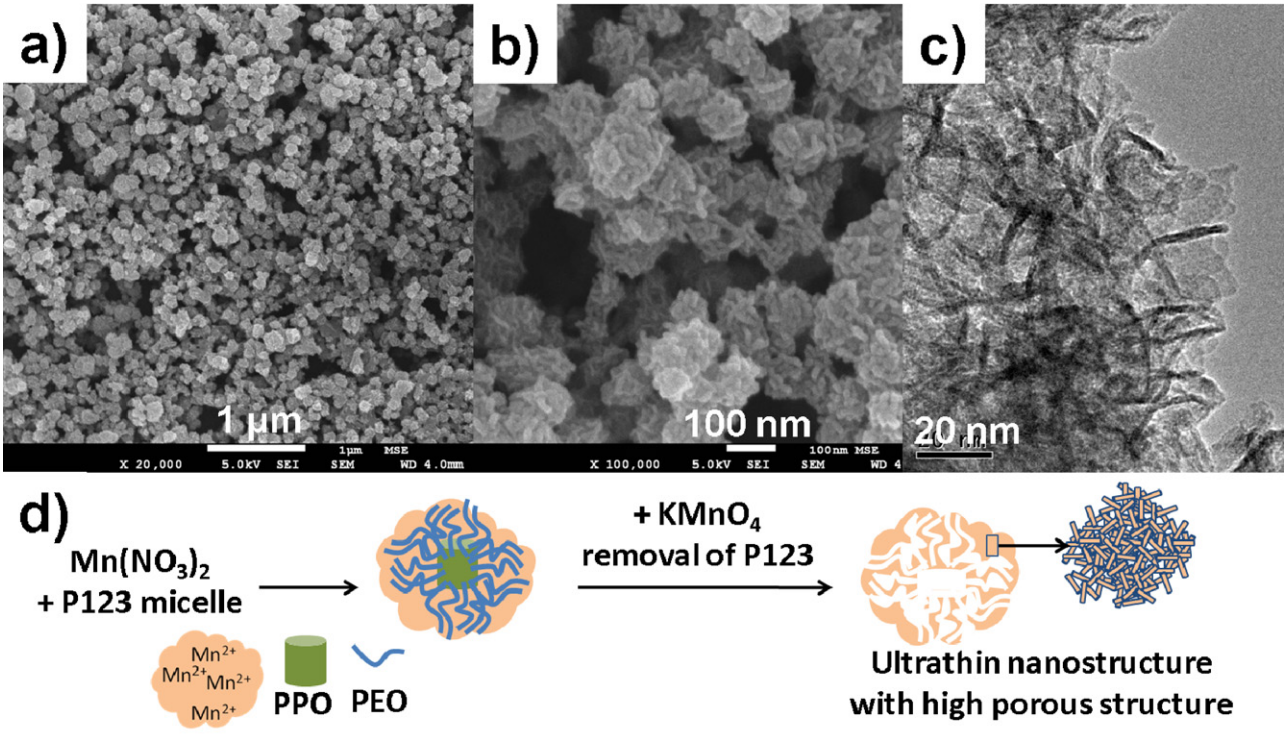

Fig. 1. (a–c) SEM and TEM images of MnO_2 sample indicate the presence of ultrathin nanostructures. (d) Schematic of synthesis of ultrathin hydrated α-MnO_2 nanostructure from P123 micelle template.

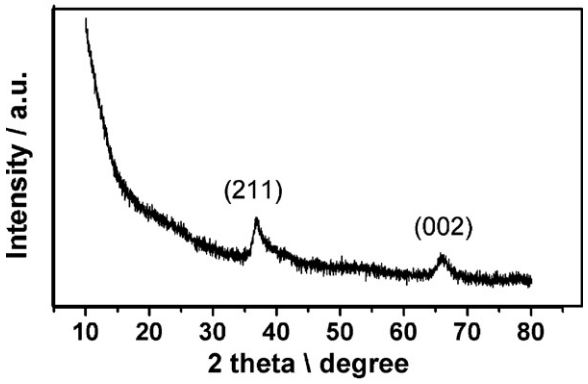

Fig. 2. XRD pattern of the as synthesized MnO_2 powder.

coalescence due to the lack of nucleation template, resulting in non-uniform and larger sphere size with less porous structure. The porous and small spheres of ultrathin nanorods are beneficial for the charge storage process as this will result in shorter ionic diffusion length which enables the device to achieve fast charge transfer rates.

The XRD pattern (Fig. 2) of the MnO_2 powders after removal of P123 template can be indexed as tetragonal α $MnO_2{\cdot}3H_2O$ (JCPDS 44-0140) [26]. The presence of hydrates is confirmed by the thermogravimetric analysis (TGA) which shows significant weight loss upon heating (Supplementary Materials Fig. 1S). Due to different arrangement of MnO_6 octahedra, MnO_2 can occur in several crystallographic forms. Among them, the α phase has been one of the preferred choices due to its large tunnel size (4.6 Å × 4.6 Å) which can accommodate more cations during the charge and discharge process as compared to alternative crystal structures, thus leading to high specific capacitance [21].

3.2. SECM study of MnO_2

In order to study the charge transfer in the MnO_2 electrodes, UME and substrate cyclic voltammetry (CV) have been carried out by using SECM. In the UME CV, the UME potential E_T is scanned within certain potential range and the current detected i_T at the UME is recorded. In this mode, the substrate or sample can be held at a certain potential E_S and the distance d between UME and substrate can be varied as well. On the other hand, the SECM substrate voltammetry is similar to normal cyclic voltammetry measurement with the exception of the SECM ability to perform the localized measurement of products released or formed at the sample. In this mode, the E_S is scanned within a certain potential range, the UME is held at a constant potential E_T, while the currents detected at the substrate (i_S) and/or UME (i_T) are recorded. Both techniques are particularly useful for identification of ion insertion or studying the kinetic barrier properties of surface modified electrode [9,29,30].

Fig. 3a shows the UME CV of the 1 mM $[Fe(CN_6)]^{3-}$ solution containing 0.1 M KNO_3 when the UME is far away from the MnO_2 substrate. It shows the known sigmoidal response for the uncomplicated reduction of $[Fe(CN_6)]^{3-}$ in the solution at potential less than 0.2 V vs. AgQRE. The UME CV scan was also performed in the proximity of the MnO_2 substrate at different d while keeping the substrate potential E_S at −0.7 V (Fig. 3b). When the E_T is negative, no current can be detected by the UME because the MnO_2 substrate competes with the UME for $[Fe(CN_6)]^{3-}$, as the potential at both UME and sample favors the reduction of $[Fe(CN)_6]^{3-}$. On the other hand, when E_T is swept to the positive range while the MnO_2 substrate is held at −0.7 V, the current was observed at the UME due to the oxidation of $[Fe(CN)_6]^{4-}$. The anodic UME current is observed to be higher when d is larger which is due to the reduced hindered diffusion process. When the substrate is held at −0.7 V, $[Fe(CN)_6]^{4-}$ ions will be generated in abundance and a macroscopic diffusion layer will develop at the slow scan rates employed. The oxidation of the sample-generated $[Fe(CN)_6]^{4-}$ at the UME is then only slightly

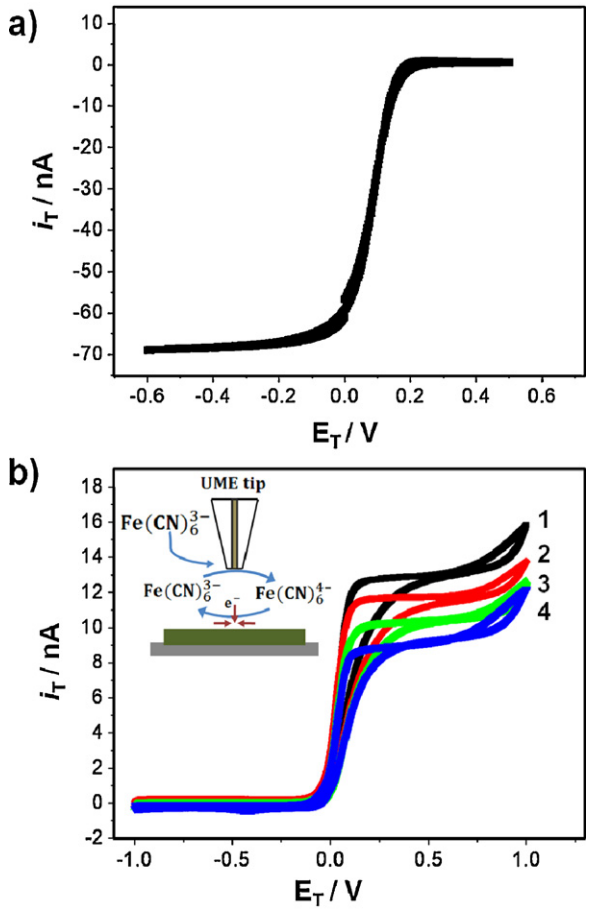

Fig. 3. (a) Sigmodial response of the UME 1 mM $[Fe(CN_6)]^{3-}$ + 0.1 M KNO_3 solution; (b) UME CV for MnO_2-coated graphite substrate with $E_S = -0.7$ V at different d. (1) 50 μm; (2) 10 μm; (3) 5 μm; (4) 1 μm; $\nu = 5$ mV s^{-1}. Inset shows the schematic of redox reaction of the mediator when UME positioned near to the MnO_2 substrate.

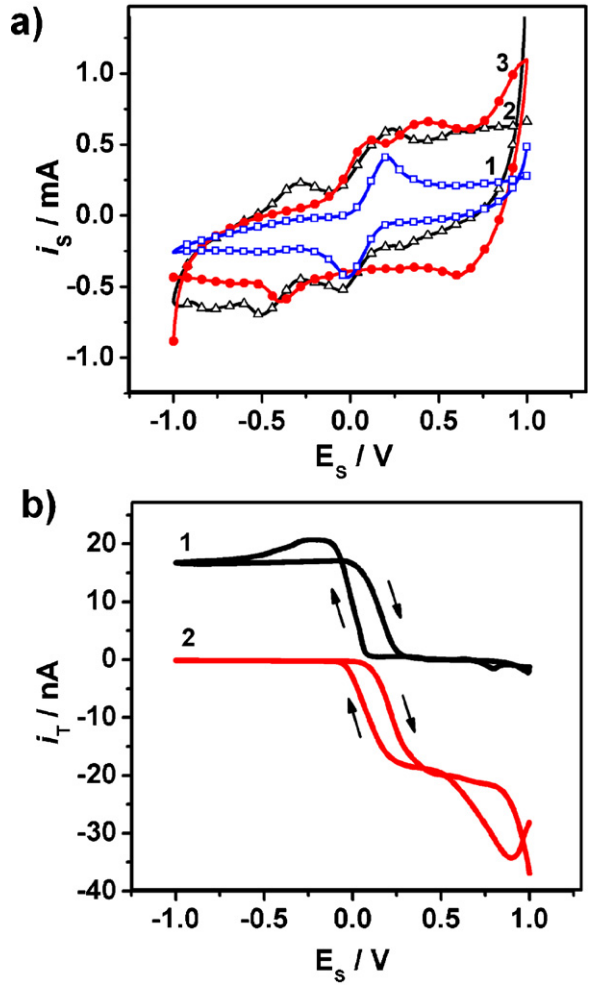

Fig. 4. (a) Cyclic voltammogram for: (1) bare carbon, (2) MnO_2-coated carbon in 1 mM $[Fe(CN_6)]^{3-}$ + 0.1 M KNO_3 solution. For comparison the CV of MnO_2-coated carbon in 0.1 M KNO_3 solution is shown in curve 3; $\nu = 20$ mV s^{-1}; (b) UME currents during a substrate CV with E_S between −1 and +1 V CV and $E_T = +0.6$ V (curve 1) and $E_T = -0.7$ V (curve 2).

influenced by d. Larger d allow lateral diffusion of $[Fe(CN)_6]^{4-}$ to contribute slightly to i_T. It is noteworthy that at a larger d, i_T shows increasing separation between the two half cycles. This is related to the increasing time required for the $[Fe(CN)_6]^{4-}$ to diffuse from the sample to the UME [7].

The substrate CV are shown in Fig. 4a shows the substrate CV at 20 mV s^{-1} obtained on the bare carbon paper and after coating a layer of MnO_2. The UME was positioned far away from the MnO_2 or carbon substrate so that it did not influence the response. $[Fe(CN)_6]^{3-}$ is reduced as expected in a one electron process as indicated by the presence of redox waves in both substrate CVs. The oxidation wave was observed around 0.24 V and the reduction wave was observed at 0 V. The overall higher currents in the CV of the MnO_2-coated sample indicate the better capacitive behavior in the MnO_2 as compared to carbon substrate.

In order to monitor the reaction of redox active $[Fe(CN)_6]^{3-}/[Fe(CN)_6]^{4-}$ ions, the UME is positioned close to the MnO_2-coated carbon substrate and held at $E_T = +0.6$ V and $E_T = -0.7$ V (Fig. 4b). UME will detect $[Fe(CN)_6]^{4-}$ when $E_T = +0.6$ V and $[Fe(CN)_6]^{3-}$ when $E_T = -0.7$ V. When $E_S = +0.6$ V, i_T is zero at positive substrate potentials as there is no reduction of $[Fe(CN)_6]^{3-}$ at the substrate, thus no $[Fe(CN)_6]^{4-}$ is formed. However, when the substrate is swept to negative potentials, a rise in i_T is observed due to the reduction of $[Fe(CN)_6]^{3-}$ to $[Fe(CN)_6]^{4-}$ at the MnO_2 surface. On the other hand, when $E_T = -0.7$ V, no UME current is observed at negative E_S due to the competition of UME and MnO_2 substrate for reduction of $[Fe(CN)_6]^{3-}$. However, when the E_S is swept to positive values the $[Fe(CN)_6]^{3-}$ added to the solution bulk is stable at the sample and $[Fe(CN)_6]^{4-}$ formed during the cathodic potential excursion is re-oxidized. The observed UME current is caused in this situation by the reduction of $[Fe(CN)_6]^{3-}$ at the UME. This shows that the MnO_2-coated carbon electrodes can still support electron transfer reaction to dissolved redox couples such as $[Fe(CN)_6]^{3-}/[Fe(CN)_6]^{4-}$.

Approach curves in the SECM feedback mode are used to study the kinetics of the charge transfer process of the MnO_2-coated carbon substrate electrodes (Fig. 5). The results are given in normalized coordinates I_T vs. L. I_T is the normalized i_T by the steady state diffusion-controlled UME current $i_{T,\infty}$ in the bulk solution, while L is the normalized d by the UME radius r_T. When the UME ($E_T = -0.5$ V) approached the MnO_2 substrate at open circuit potential (OCP), an enhanced steady state current (positive feedback) was observed. The current–distance curve can be fitted well to the analytical approximation by Cornut and Lefrou for finite sample kinetics by changing the normalized heterogeneous rate constant κ [27]. The effective heterogeneous rate constant is calculated according to the following equation $k_{eff} = \kappa D/r_T$. Taking the diffusion coefficient $D = 7 \times 10^{-5}$ cm^2 s^{-1} and $r_T = 6.28$ μm, the k_{eff} values are found as 1.2×10^{-2} cm s^{-1} for the bare carbon substrate, 8.3×10^{-3} cm s^{-1} for the MnO_2-coated substrate at OCP, 3.0×10^{-3} cm s^{-1} for the MnO_2 substrate biased at 0 V and 8.9×10^{-4} cm s^{-1} for the MnO_2

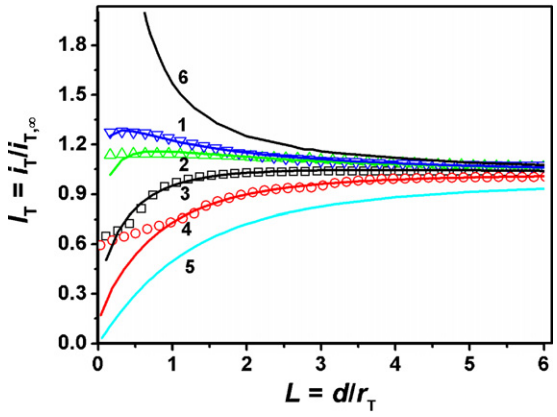

Fig. 5. SECM approach at $E_T = -0.5$ V in 1 mM $K_3[Fe(CN)_6]$ + 0.1 M KNO_3 towards (1) bare carbon substrate at open circuit potential (OCP), (2) MnO_2-coated carbon substrate at OCP, (3) MnO_2-coated carbon substrate at $E_S = 0$ and (4) MnO_2-coated carbon substrate at E_S −0.24 V. Experimental data are given as open symbols, fits to the theory [26] are shown as the solid lines. The theory for pure hindered diffusion (curve 5) and diffusion controlled mediator recycling (curve 6) are given for comparison.

substrate biased at −0.24 V. These values are higher as compared to the heterogeneous rate constant of the glassy carbon electrode modified nitrobenzenediazonium salt [31] and comparable to the boron doped diamond and indium tin oxide (ITO) electrodes [4]. In addition, these data are also in the range of the macroscopic reaction rate constants measured using conventional cyclic voltammetry in similar electrolyte on the monolayer graphene surface [32] and TiO_2/carbon core shell nanofibers [33], indicating the effectiveness of MnO_2 as the electrode material for the electrochemical based devices.

The rate constant is the highest on the bare carbon substrate because carbon is a better electron conductor than MnO_2. At OCP (i.e. 0.05 V vs. AgQRE) an electron is transferred from $[Fe(CN)_6]^{4-}$ to the MnO_2 (Eq. (1)). Once the charge transfer occurs, there can be lateral diffusion of charges due to surface conductivity of MnO_2. The nanostructure of MnO_2 helps to facilitate the charge transfer process at the interfaces as it provides large surface area and porosity for effective contact between the electrolyte and MnO_2.

$$[Fe(CN)_6]^{4-} \rightarrow [Fe(CN)_6]^{3-} + e^- \quad (1)$$

Alternatively, when MnO_2 substrate is held at 0 V, MnO_2 itself consumes the $[Fe(CN)_6]^{3-}$ ions in the electrolyte solution as the reduction of $[Fe(CN)_6]^{3-}$ to $[Fe(CN)_6]^{4-}$ happens at potential <0.2 V vs. AgQRE. This results in reduced diffusion of $[Fe(CN)_6]^{3-}$ to UME, resulting in the low UME current. Further shifting the potential of the MnO_2 substrate towards the negative side (i.e. −0.24 V), results in more consumption of $[Fe(CN)_6]^{3-}$ ions in the solution. This leads to lower UME current and therefore lower effective rate constant are observed in MnO_2 held at −0.24 V as compared to the MnO_2 held at 0 V as well as the one without externally applied potential.

As the thickness of the MnO_2 coating is about 18 μm, the extent of positive feedback that occurs on the MnO_2-coated carbon substrate at the open circuit potential is solely based on the electron transfer kinetics at the interface of electrolyte/MnO_2 and the contribution from the direct reduction of $[Fe(CN)_6]^{3-}$ at the carbon substrate was negligible. Thus, the presence of positive feedback current must be due to the favorable charge transfer process into the MnO_2 electrode. This is attributed to the desired physical properties of MnO_2 electrode. The presence of porous ultrathin nanostructures provides direct and large accessible surface area for the charge transfer process to take place. The morphology of the electrode has been reported to be an important factor in determining the kinetic process and electrochemical activity of the electrode [33]. The facile charge transfer process of this material fits one of the key requirements essential for supercapacitor device. Therefore, pseudocapacitive properties of the MnO_2 are further examined by the conventional three electrode test to assess its capability as supercapacitor electrode.

3.3. Pseudocapacitive performance and electrochemical impedance spectroscopy of MnO_2

Charge storage mechanisms of MnO_2 are based on two processes, intercalation/deintercalation and surface process. The energy conversion and storage capability of MnO_2 mainly stems from its ability to give fast and reversible redox reactions between Mn(III) and Mn(IV) with the intercalation of protons or alkali metal cations such as Na^+, K^+ or Li^+ in the bulk upon reduction followed by deintercalation upon oxidation. Adsorption of electrolyte cations on the MnO_2 surfaces accounts for the alternative process [24,25,34,35]. The contribution from each type of charge storage mechanism depends on the crystal structure, water content, surface area, porosity and intercalated cations [21,36,37].

The pseudocapacitive properties of MnO_2 samples were studied using a conventional three electrode test measurement in 1 M Na_2SO_4. Fig. 6a shows the galvanic charge and discharge cycle of the MnO_2 samples. The linear potential signal within the 0.9 V potential window from 0 to 0.9 V vs. Ag/AgCl reference electrode for all applied current indicates the pseudocapacitive nature of the materials [38]. Furthermore, cyclic voltammograms of MnO_2 sample at different scan rate during cyclic voltammetry test are shown in Fig. 6b. The rectangular shape of CV scan, especially at 10 mV s^{-1} shows the pseudocapacitive properties of MnO_2 due to the fast and reversible surface redox reactions of MnO_2 [19]. The specific capacitance (C_{sp}) of the electrode materials is calculated from the galvanic charge–discharge test: $C_{sp} = (i \times \Delta t)/(m \times \Delta V)$, where i is the current applied, Δt is the discharge time, m is the active mass of the electrode, and ΔV is the voltage window of the test, in this case is 0.9 V. The calculated C_{sp} at applied current of 2, 5 and 10 A g^{-1} is about 357, 269 and 184 F g^{-1}, respectively.

Theoretically, C_{sp} of MnO_2 is able to reach more than 1300 F g^{-1} for one electron transfer due to Mn(III)/Mn(IV) transition within 0.9 V operating window [24]. Due to the shortened diffusion distance for solid state transport of ions, ultrathin layer deposition of MnO_2 with the thickness of tens of nm or loading mass of up to tens of μg has given rise to C_{sp} of more than 2000 F g^{-1} [24,25,39]. Therefore, the comparison of the gravimetric capacitance among the MnO_2 electrodes in the literatures will only be fair for electrodes with similar loading mass [40]. The C_{sp} of our sample at 2 Ag^{-1} is better as compared to those electrodes with similar loading mass (100–500 μg cm^{-2}), giving C_{sp} in the range of 170–306 F g^{-1} [21,41–46]. Furthermore, continuous charge and discharge test at 2 A g^{-1} of our sample shows almost no degradation after 2000 cycle of cycling test, indicating the favorable long term stability of our sample (Fig. 6c).

Electrochemical impedance spectroscopy (EIS) measurements were also carried out in order to understand the relationship between the SECM kinetics data of the MnO_2 electrode and its capacitive performance. Fig. 6d shows the Nyquist plot of MnO_2 sample from the EIS measurement in 1 M Na_2SO_4 at constant voltage mode of 0.2 V vs. Ag/AgCl. The inset Fig. 6d shows the semicircular part of the curve of the high frequency range. In order to extract the value of impedance parameters, the Nyquist plot is fitted to the respective electronic circuit model shown in Fig. 6d. R_s represents the electrolyte resistance which is equivalent to high frequency intercept on the Z real or X axis. The depressed semicircle at the high frequency region is related to the characteristics of the double layer or surface capacitance C_{dl} as well as charge transfer resistance R_{ct} which can be extracted from the diameter of the

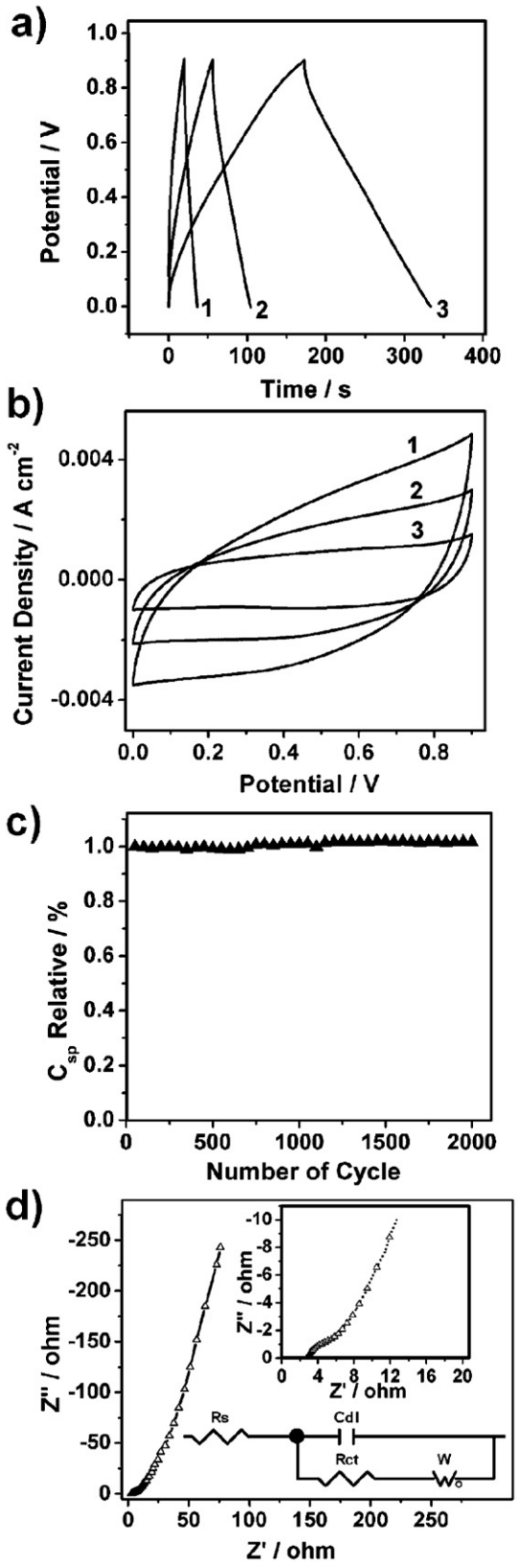

Fig. 6. (a) Galvanic charge and discharge cycle of MnO_2 at: (1) 10 A g^{-1}; (2) 5 A g^{-1}; (2) 2 A g^{-1}; (b) Cyclic voltammogram of MnO_2 measured at (1) 50 mV s^{-1}; (2) 25 mV s^{-1}; (3) 10 mV s^{-1}; (c) C_{sp} relative of MnO_2 during the extended charge and discharge test for 2000 cycle at 2 A g^{-1}; (d) Nyquist plots of MnO_2. Inset shows the enlarged scale at high frequency region and equivalent circuit model. All the measurements were performed in 1 M Na_2SO_4.

semicircle arc. Warburg impedance W is extracted from the low frequency region which depicts the diffusion process of electrolyte ion into the active materials. For ideal capacitive behavior, the line in the low frequency region should be parallel to the imaginary Z axis forming a 90° slope [44,46]. The experimental slope is closer to 90° which indicates a predominately capacitive behavior. At high frequency region, the low intercept at the Z real axis (2.9 Ω) indicates the small R_s of the MnO_2 sample. Besides that, the calculated R_{ct} from the fitting result (0.639 Ω) also represents the low charge transfer resistance on the surface of the MnO_2 electrode in contact with electrolyte. Therefore, the low charge transfer and ionic resistance of the MnO_2 electrode are consistent with the enhanced kinetics process found during the SECM measurement.

The exemplary C_{sp} of MnO_2 measured by the three electrode test is directly related to the superior electrochemical kinetics of MnO_2, quantified by the SECM effective heterogeneous rate constant. Poor kinetics process can lead to the high resistance of the electrode and results in an inferior pseudocapacitive performance of the supercapacitor device. Positive feedback observed during the SECM measurement indicates the favorable charge transfer process at the interface of the MnO_2 electrode and electrolyte, thus giving rise to high C_{sp}. Nanostructure in porous configuration has been shown to have better performance due to the presence of large available contact area which will improve the ion migration pathway as well as adsorption/desorption process of electrolyte ions [20]. C_{sp} of MnO_2 has found to be affected by ionic conductivity and accessible surface area of the electrode materials [21,36]. Accessibility of the electrolyte ions through the bulk structure has been reported to be a more crucial factor in optimizing the C_{sp} of pseudocapacitive materials as compared to the Brunauer–Emmett–Teller (BET) surface area [36]. The efficient transport of the electrolyte ions is related to the high ionic conductivity which can be seen from the EIS data. It is also affected by the morphology of the electrode, typically the pore volume and structure of the material.

The BET measurement shows that the resultant MnO_2 has narrow pore size distribution of 3–4 nm (Supplementary Materials Fig. S2), this can be classified as mesoporous structure. Due to the lack of structural regularity observed under TEM investigation, it can be described as disordered mesoporous within the interleaving and hierarchical nanostructures. The BET surface area and the total pore volume of the MnO_2 sample is about 336 m^2 g^{-1} and 0.54 cm^3 g^{-1}, respectively. The isotherm plot reveals a strong hysteresis loop in the relative pressure range of 0.4–1 indicating the characteristic of adsorption and desorption process of the porous materials (Supplementary Materials Fig. S3). To the best of our knowledge, our MnO_2 has the highest surface area and pore volume as compared to other crystalline MnO_2 reported so far [20,21,28,36,47–49]. The large pore volume indicates the open structure of our sample due to the presence of block copolymer template during the synthesis. This results in the good accessibility of the electrolyte ions and low ionic resistance as found in the enhanced kinetics process during the SECM measurement as well as the commendable pseudocapacitive performance of the MnO_2 electrode. In addition of the open structure and crystalline nature of α MnO_2, the presence of hydrates in our MnO_2 help to improve the charge storage process as it enhances the diffusion of H^+ and Na^+ via hopping process within H_2O and OH^- sites, providing the sites for rapid charge transfer and cation diffusion process [50].

4. Conclusions

High specific capacitance has been achieved due to the presence of effective charge transport process at the interface of MnO_2 and electrolyte as well as the presence of porous ultrathin nanostructure and α hydrated compound. The high kinetics of the

charge transfer processes is evident from the Nyquist plots of the MnO_2 electrodes which show low series and charge transfer resistances. This is also evident from measurements using the scanning electrochemical microscopy with $[Fe(CN)_6]^{4-}/[Fe(CN)_6]^{3-}$ as redox mediator that has been applied for the first time to study processes at the supercapacitor electrode. Positive feedback current has been observed during the SECM approach curve, indicating the efficient charge transfer process into the MnO_2 electrode which is highly essential for high performance supercapacitor device.

Acknowledgements

A. Sumboja and U.M. Tefashe are grateful to the scholarships funded by Nanyang Technological University (Singapore) and German Academic Exchange Service (DAAD, Germany). P.S. Lee acknowledges the fellowship awarded by the Hanse Institute of Advanced Studies, Delmenhorst, Germany in supporting this work.

Appendix A. Supplementary data

Supplementary data associated with this article can be found, in the online version, at doi:10.1016/j.jpowsour.2012.01.153.

References

[1] S.V. Kalinin, N. Balke, Adv. Mater. 22 (2010) E193–E209.
[2] R.C. Tenent, D.O. Wipf, J. Solid State Electrochem. 13 (2009) 583–590.
[3] M. Arca, M.V. Mirkin, A.J. Bard, J. Phys. Chem. 99 (1995) 5040–5050.
[4] A.K. Neufeld, A.P. O'Mullane, J. Solid State Electrochem. 10 (2006) 808–816.
[5] A.W. Taylor, F.L. Qiu, J.P. Hu, P. Licence, D.A. Walsh, J. Phys. Chem. B 112 (2008) 13292–13299.
[6] G. Wittstock, M. Burchardt, S.E. Pust, Y. Shen, C. Zhao, Angew. Chem. Int. Ed. 46 (2007) 1584–1617.
[7] J. Kwak, F.C. Anson, Anal. Chem. 64 (1992) 250–256.
[8] J. Kwak, A.J. Bard, Anal. Chem. 61 (1989) 1221–1227.
[9] C. Lee, F.C. Anson, Anal. Chem. 64 (1992) 528–533.
[10] I. Turyan, B. Orel, R. Reisfeld, D. Mandler, Phys. Chem. Chem. Phys. 5 (2003) 3212–3219.
[11] N.R. Wilson, M. Guille, I. Dumitrescu, V.R. Fernandez, N.C. Rudd, C.G. Williams, P.R. Unwin, J.V. Macpherson, Anal. Chem. 78 (2006) 7006–7015.
[12] C. Lee, A.J. Bard, Anal. Chem. 62 (1990) 1906–1913.
[13] S.B. Basame, H.S. White, Anal. Chem. 71 (1999) 3166–3170.
[14] N.J. Yang, C.G. Zoski, Langmuir 22 (2006) 10338–10347.
[15] Y. Shen, U.M. Tefashe, K. Nonomura, T. Loewenstein, D. Schlettwein, G. Wittstock, Electrochim. Acta 55 (2009) 458–464.
[16] U.M. Tefashe, T. Loewenstein, H. Miura, D. Schlettwein, G. Wittstock, J. Electroanal. Chem. 650 (2010) 24–30.
[17] P. Bertoncello, Energy Environ. Sci. 3 (2010) 1620–1633.
[18] K.R.J. Lovelock, F.N. Cowling, A.W. Taylor, P. Licence, D.A. Walsh, J. Phys. Chem. B. 114 (2010) 4442–4450.
[19] P. Simon, Y. Gogotsi, Nat. Mater. 7 (2008) 845–854.
[20] D.W. Liu, B.B. Garcia, Q.F. Zhang, Q. Guo, Y.H. Zhang, S. Sepehri, G.Z. Cao, Adv. Func. Mater. 19 (2009) 1015–1023.
[21] S. Devaraj, N. Munichandraiah, J. Phys. Chem. C 112 (2008) 4406–4417.
[22] H.Y. Lee, J.B. Goodenough, J. Solid State Chem. 144 (1999) 220–223.
[23] H.Y. Lee, V. Manivannan, J.B. Goodenough, C.R. Acad, Sci Paris, t-2, Serie II c 2 (1999) 565–577.
[24] M. Toupin, T. Brousse, D. Belanger, Chem. Mater. 16 (2004) 3184–3190.
[25] S.C. Pang, M.A. Anderson, T.W. Chapman, J. Electrochem. Soc. 147 (2000) 444–450.
[26] J. Wang, E. Khoo, J. Ma, P.S. Lee, Chem. Commun. 46 (2010) 2468–2470.
[27] R. Cornut, C. Lefrou, J. Electroanal. Chem. 621 (2008) 178–184.
[28] R.R. Jiang, T. Huang, J.L. Liu, J.H. Zhuang, A.S. Yu, Electrochim. Acta 54 (2009) 3047–3052.
[29] M.H.T. Frank, G. Denuault, J. Electroanal. Chem. 354 (1993) 331–339.
[30] M.H.T. Frank, G. Denuault, J. Electroanal. Chem. 379 (1994) 399–406.
[31] S. Griveau, S. Aroua, D. Bediwy, R. Cornut, C. Lefrou, F. Bedioui, J. Electroanal. Chem. 647 (2010) 93–96.
[32] A.T. Valota, I.A. Kinloch, K.S. Novoselov, C. Casiraghi, A. Eckmann, E.W. Hill, R.A.W. Dryfe, ACS Nano 5 (2011) 8809–8815.
[33] R. Chen, L. Hu, K. Huo, J. Fu, H. Ni, Y. Tang, P.K. Chu, Chem. Eur. J. 17 (2011) 14552–14558.
[34] J.W. Long, D. Belanger, T. Brousse, W. Sugimoto, M.B. Sassin, O. Crosnier, MRS Bull. 36 (2011) 513–522.
[35] D. Belanger, T. Brousse, J.W. Long, Electrochem. Soc. Interface 17 (2008) 49–52.
[36] O. Ghodbane, J.L. Pascal, F. Favier, In ECS Transactions, vol. 16, 1st ed., 2008, pp. 235–241.
[37] T. Brousse, M. Toupin, R. Dugas, L. Athouel, O. Crosnier, D. Belanger, J. Electrochem. Soc. 153 (2006) A2171–A2180.
[38] T. Shinomiya, V. Gupta, N. Miura, Electrochim. Acta 51 (2006) 4412–4419.
[39] A. Cross, A. Morel, A. Cormie, T. Hollenkamp, S. Donne, J. Power Sources 196 (2011) 7847–7853.
[40] Y. Gogotsi, P. Simon, Science 334 (2011) 917–918.
[41] C.C. Hu, C.C. Wang, J. Electrochem. Soc. 150 (2003) A1079–A1084.
[42] N. Nagarajan, M. Cheong, I. Zhitomirsky, Mater. Chem. Phys. 103 (2007) 47–53.
[43] C.C. Hu, Y.T. Wu, K.H. Change, Chem. Mater. 20 (2008) 2890–2894.
[44] S. Devaraj, N. Munichandraiah, J. Electrochem. Soc. 154 (2007) A80–A88.
[45] J.N. Broughton, M.J. Brett, Electrochim. Acta 50 (2005) 4814–4819.
[46] W. Xiao, H. Xia, J.Y.H. Fuh, L. Lu, J. Electrochem. Soc. 156 (2009) A627–A633.
[47] M. Xu, L. Kong, W. Zhou, H. Li, J. Phys. Chem. C 111 (2007) 19141–19147.
[48] V. Subramanian, H. Zhu, R. Vajtai, P.M. Ajayan, B. Wei, J. Phys. Chem. B 109 (2005) 20207–20214.
[49] G.R. Li, Z.P. Feng, Y.N. Ou, D.C. Wu, R.W. Fu, Y.X. Tong, Langmuir 26 (2010) 2209–2213.
[50] M. Ghaemi, F. Ataherian, A. Zolfaghari, S.M. Jafari, Electrochim. Acta 53 (2008) 4607–4614.